Magmatism Controls Global Oceanic Transform Fault Topography

Xiaochuan Tian
x.tian@bc.edu

Boston College https://orcid.org/0000-0003-0289-1794

Mark Behn
Boston College https://orcid.org/0000-0002-2001-1335

Garrett Ito
University of Hawaii

Jana Schierjott
UH https://orcid.org/0000-0002-8596-9851

Boris Kaus
Institute of Geosciences & Computational Sciences Mainz, University of Mainz https://orcid.org/0000-0002-0247-8660

Anton Popov
Uni Mainz

Article

Keywords:

Posted Date: September 18th, 2023

DOI: https://doi.org/10.21203/rs.3.rs-3286998/v1

Additional Declarations: There is **NO** Competing Interest.

Version of Record: A version of this preprint was published at Nature Communications on March 1st, 2024. See the published version at https://doi.org/10.1038/s41467-024-46197-9.

Title: Magmatism Controls Global Oceanic Transform Fault Topography

Author list: Xiaochuan Tian[1]*, Mark D. Behn[1], Garrett Ito[2], Jana Schierjott[2], Boris J. P. Kaus[3], Anton A. Popov[3]

Affiliations:

[1] Department of Earth and Environmental Sciences, Boston College; Chestnut Hill, MA 02467, US.

[2] Department of Earth Sciences, University of Hawaii; Honolulu, Hawaii 96822, US.

[3] Institute of Geosciences, Johannes Gutenberg University Mainz; Mainz, 55128, Germany.

*Corresponding author. Email: x.tian@bc.edu

Abstract:

Oceanic transform faults are fundamental features of plate tectonics, accommodating strike-slip motion between two adjacent mid-ocean ridge segments. The continuations of these faults form tectonically inactive fracture zones, creating the longest 'scars' on the Earth's surface. Yet, despite the relatively simple kinematic and thermal structures, oceanic transform faults display an enigmatic continuum of morphologies ranging from deep valleys to small ridges. Here, through three-dimensional numerical modeling of two mid-ocean ridge segments separated by a transform fault, we find that the rate of magma intrusion within the transform domain exerts a first-order control on transform topography. Low-rate magmatism results in transform-parallel tectonic stretching, generating deep transform valleys and fracture zones. Intermediate-rate magmatism fully accommodates far-field stretching, but strike-slip motion induces across-transform tension, producing shallow valleys whose depth increases with the shear strength of the fault. High-rate magmatism leads to local compression that generates fault-parallel ridges. The models not only reproduce the observed global transform valley depths but also predict the observation that fracture zones are consistently shallower than their adjacent transform valleys. These results suggest that plate motion changes are not a necessary condition for generating oceanic transform topography and that oceanic transform faults are not simple conservative strike-slip plate boundaries.

Main text:

Oceanic transform faults display a wide range of topographic morphologies that broadly correspond to the spreading rate of the adjacent mid-ocean ridge. At the fastest seafloor spreading rates, transform morphology is often variable, with low-relief (hundred-meter) transform ridges that run parallel to the transform fault (Mode 1, Fig. 1a). At fast to intermediate spreading rates, shallow valleys with less than 1 km of relief delineate the fault zone (Mode 2, Fig. 1b). Finally, at slow to ultra-slow spreading ridges, deep (>1 km) transform valleys form and the corresponding fracture zones are deeper than the adjacent seafloor (Mode 3, Fig. 1c). Another global observation is that fracture zones are consistently shallower than their adjacent transforms by an average of ~650 meters [1]. Although a systematic relationship between spreading rate and the morphology of mid-ocean ridges is well documented and understood to be related to differences in magma supply [2,3], the cause of the spectrum in oceanic transform topography, and its contrast with the adjacent fracture zones, is still not clear ~60 years after they were first discovered [4,5].

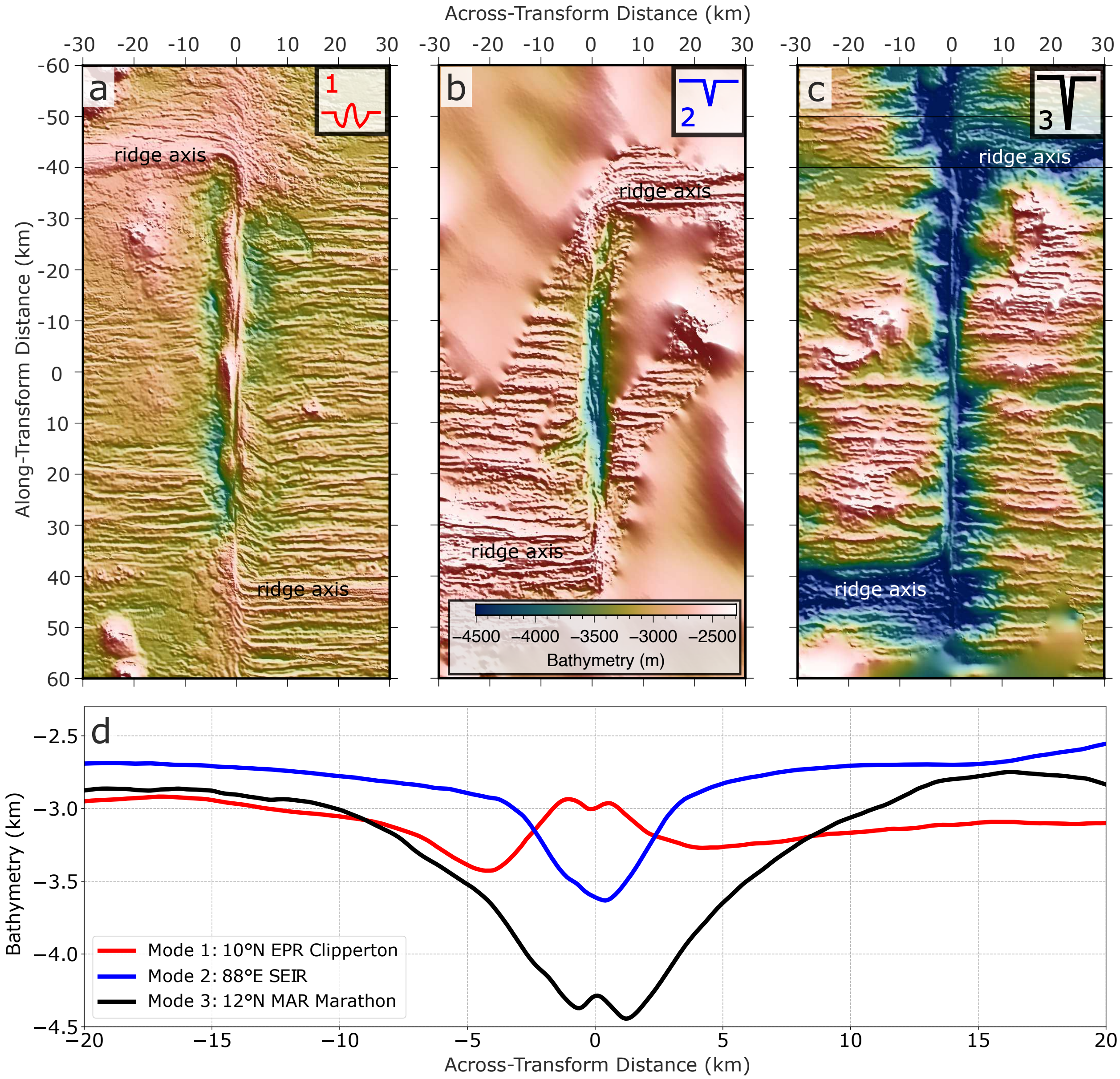

Fig. 1. Characteristic bathymetry and transform-perpendicular averaged bathymetric profiles for the 3 major modes of transform fault morphologies. (**a**) Mode 1 ridge at 10°N East Pacific Rise (EPR), Clipperton Transform Fault with a full spreading rate of 103.4 mm/yr; (**b**) Mode 2 intermediate valley at 88°E Southeast Indian Ridge (SEIR) with a full spreading rate of 65.4 mm/yr; and (**c**) Mode 3 deep valley at 12°N Mid-Atlantic Ridge (MAR), Marathon Transform Fault with a full spreading rate of 24.5 mm/yr. (**d**) Averaged across-transform topography for each mode shown in (a), (b) and (c). Bathymetry data from

ref [6]. Plotted with GMT [7]. The bathymetry maps are rotated so that all transform faults have the same up-down orientation.

Prior models for transform fault morphology

Two mechanisms are frequently invoked to explain transform fault morphology. The first suggests that plate motion changes generate transform-perpendicular compression or extension leading to the formation of transform ridges or valleys, respectively [8,9]. However, plate motion changes are not persistent in time and some transform ridges and valleys arise without significant plate motion changes, suggesting other fundamental causes. An alternative model invokes the nonlinear viscoelastic response due to the shearing of two adjacent plates to explain the observed transverse ridges that bound the transform valleys [10]. This model relates transform valley depth to fault shear stress but does not explain the observed spreading rate dependence of transform valley depth, nor the depth difference between fracture zones and transform valleys.

One important property of mid-ocean ridges that is known to vary with spreading rate is magma supply [11]. Seismic, gravity, and bathymetric observations at the slow-spreading Mid-Atlantic ridge show evidence for thinner crust along transform faults and fracture zones, indicating lower magma supply [12–14]. These observations suggest reduced extension via magmatic intrusions (dikes) and enhanced extension via tectonic faulting near the adjoining ends of the ridge segments, as compared to the segment centers [2,15–17]. By contrast, gravity data at fast-spreading mid-ocean ridges show evidence for thicker crust along transform faults [13], indicating enhanced magmatism. Because spreading-rate dependent magma supply [11] is well known to affect ridge axis topography through its control on lithospheric thickness and fault style [2,18–22], variations in magma supply may also influence transform fault morphologies. Consistent with this idea, a recent study showed bathymetric evidence for magmatism extending across the transform fault domain, and linked this to the observed shallowing of fracture zones relative to their adjacent transform valleys [1].

3-D transform models incorporating magma intrusion

Here, we construct three-dimensional (3-D) numerical models using the finite difference code LaMEM [23] to investigate the origin of oceanic transform topography and its relationship to magma supply (see Method for details). The models simulate a ridge-transform-ridge spreading system with a 6-km thick lithospheric plate and elasto-visco-plastic rheology (Fig. 2). Seafloor spreading is imposed kinematically by pulling on two opposing sides of the model domain, each at a rate Vx. Two fixed ridge segments are offset by 32 km, between which a transform fault forms spontaneously as a result of plastic deformation that follows the Drucker-Prager yield criterion. Along the ridge segments, material divergence is imposed to simulate dike intrusion, which accounts for a fraction, M, of the full spreading rate $2 \cdot Vx$ [2,15,24]. For the portion of the ridge segment outside of transform domain, $M = 1$ so that seafloor spreading is fully accommodated by dike intrusions, rather than by extensional faulting. This simplification allows us to focus on topography arising from deformation along the transform fault, which is not complicated by abyssal-hill-forming ridge-parallel normal faults [18,19,21,24].

Inspired by evidence for spreading rate dependent magma supply within oceanic transform faults (e.g., ref [1,12,13]) and high-resolution geological observations from deep-towed photographs of constructional volcanic ridges that traverse across the entire width of the fracture zone at the ridge-transform intersections of the Kane transform [25], we also implement dike intrusions along the extensions of the ridge segments within the transform domain. Here, the fraction of seafloor spreading accommodated by diking is denoted as M_T, in distinction to M, which pertains only to the ridge axes outside of the transform domain (Fig. 2b). The fractional rate of extension due to diking at each end of the transform fault is $M_T/2$, such that M_T represents the integrated opening rate within the transform domain. The transform domain width is set to be either 1 km (for fast spreading cases) or 2 km (for intermediate to slow spreading cases), which is roughly consistent with a recent bathymetric analyses [26] that yield a global median transform width of 2.5 km or 1.8 km when the corresponding ridge full spreading rate is higher than 8 cm/yr.

Using this model setup, we investigate two primary controls on transform morphology, namely, variations in (1) M_T, and (2) fault shear strength, controlled by varying cohesion C (Eq. 2 in Methods). We measure model topography on evenly spaced along- and across-fault profiles, from which we calculate the average along- and across-transform model topography (Extended Data Fig. 1 d, e, f for average along- and Extended Data Fig. 1 g, h, i for average across-transform topography for the three example cases shown in Fig. 3). Transform valley and fracture zone depths (Fig. 3d and Fig. 4a) are measured from the mean of the along-transform profiles (similar to the analysis of natural systems ref [1]), once the transform topography has reached steady state or evolve slowly, typically in ≤ 10 million years of model time.

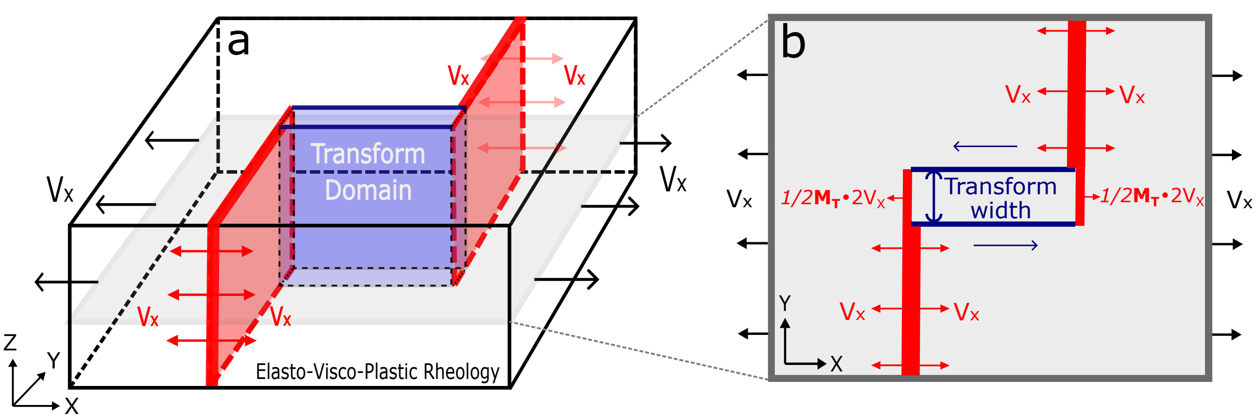

Fig. 2. Model setup. (**a**) 3-D (64×32×6 km) model domain with elasto-visco-plastic rheology. Model is composed of cubic elements with 0.5 km edge length. Left and right boundaries are pulled with a half

spreading rate of Vx = 2 cm/yr. Top boundary is open to flow in and out of a 2-km layer of "sticky air" [27,28]. The other boundaries are free of shear traction with no normal in-and-out flow. (**b**) Map view of the cross-section shaded in (a). Two ridge segments open, via diking, at the same rate of plate separation (i.e., M = 1) outside of transform domain. Within the transform domain the end of each ridge segment opens at a rate $M_T \cdot Vx$. Transform domain width is set to be either 1 or 2 km. The transform fault strength is governed by Drucker-Prager yield criterion: $\tau_Y = sin(\varphi)P + cos(\varphi)C$, where the friction angle $\varphi =$ 30°, P is lithostatic pressure and C is cohesion [23].

Predicted modes of transform morphology

The models show that transform bathymetry deepens systematically with decreasing rates of magmatic accretion (M_T) in the transform domain (Fig. 3d). From relatively high to low M_T, the models can be categorized into three main modes of transform morphology, namely, topographic ridges along the transform (Mode 1), shallow transform valleys (Mode 2), and deep transform valleys (Mode 3). These three modes reproduce the global trend of transform-valley depth vs. spreading rate, and are consistent with the observed range of transform-valley depths (Fig. 3d vs. 3e). The models also generate fracture zones that are systematically shallower than transform valleys, as observed globally (Fig. 4).

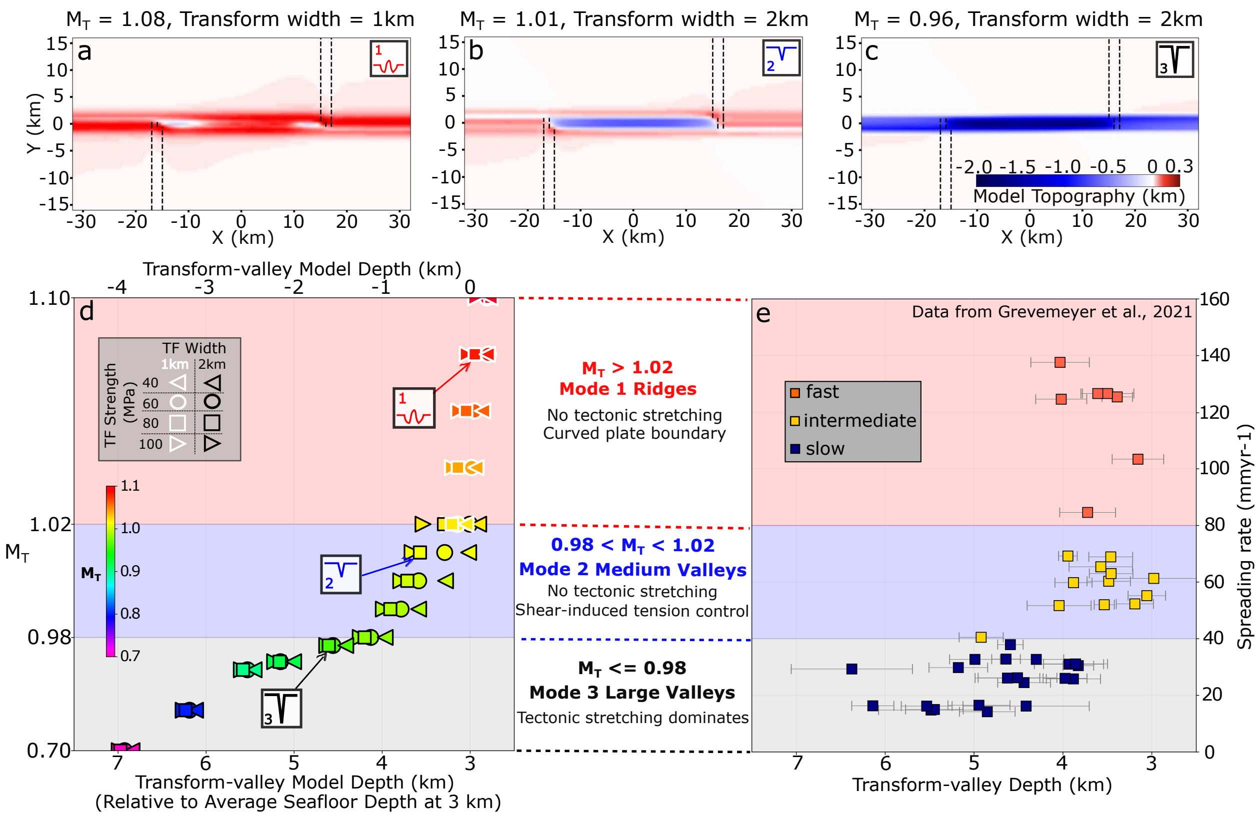

Fig. 3 | Transform fault morphology as a function of the fraction (M_T) of seafloor spreading accommodated by magmatism in the transform domain. Model topography for (**a**) a small transform ridge, (**b**) a shallow transform valley (< 1 km relief), and (**c**) a deep valley (> 1 km of relief). Black dashed lines mark the edges of the magma intrusion zones. (**d**) Model transform-valley depth as a function of M_T (symbol infill colors). Symbols denote transform fault cohesion (symbol shape) and imposed transform width (symbol outline color). Note that transform-valley model depth (top axis) is measured relative to the initial model surface depth (0 km), which is equivalent to 3 km depth on the bottom axis assuming an average seafloor depth near a ridge axis of 3 km [29–31]. Negative values along the top axis implies subsidence relative to the initial surface, whereas larger values in the bottom axis means deeper seafloor (see supplement for details). (**e**) Global observations of transform valley depth (in km below sea level) as a function of spreading rate [1]. In (d), the vertical axis height of M_T from 0.70 to 0.98 (Mode 3) is scaled by 1/7 so as to match the height of the vertical axis of spreading rate from 0–40 mm/yr in (e). This scaling follows the relationship derived by [11,21], which implies that the rate of magmatic extension, M, is lowest and most variable at the slower spreading ridges.

Mode 1 topography forms when magmatic accretion in the transform domain accommodates slightly more extension than the far-field plate separation ($M_T > 1.02$). This mode shows hundred-meter-high fault-parallel topographic ridges, sometimes separated by small depressions centered along the transform zone or near the ridge-transform intersections (Fig. 3a and Extended Data Fig. 1 a, d, g). Higher values of M_T lead to slightly taller topographic ridges (Fig. 3d Mode 1). Mode 1 is consistent with the small topographic ridges observed at some transform faults at fast-spreading ridges (Fig. 1a).

Mode 2 topography occurs when the magmatic extension rate in the transform zone approximately matches the seafloor spreading rate ($M_T = 0.98$–1.02, Fig. 3d). In these cases, there is little transform-parallel tectonic tension caused by far-field plate separation, as the extension is fully accommodated by magma intrusion. Nonetheless, this mode predicts intermediate depth (100–1000 m) transform valleys (Fig. 3b and Extended Data Fig. 1 b, e, h) that deepen with stronger transforms (Fig. 3d Mode 2 and Extended Data Fig. 2). Mode 2 is consistent with intermediate depth transform valleys observed at fast to intermediate spreading ridges where the corresponding fracture zones typically show little relief (Fig. 1b).

Finally, Mode 3 topography occurs when magmatic extension does not fully accommodate plate separation in the transform domain ($M_T < 0.98$). This leads to an increasing fraction of seafloor spreading that is accommodated by along-transform tectonic stretching with decreasing M_T (Fig. 3c & d Mode 3 and Extended Data Fig. 1 c, f, i). Mode 3 therefore produces deep valleys (1–4 km), that deepen with decreasing M_T (Fig. 3d). Compared to Mode 2, Mode 3 valley depths increase less with transform strength (Extended Data Fig. 2). Further, in contrast to the small amount of fracture zone uplift in Mode 1 and 2 models, the fracture zones in Mode 3 models are expressed as valleys, but remain ~1 km shallower than the transform valleys (Fig. 4a). Mode 3 is consistent with the deep transform and fracture zone valleys found at slow-spreading rates (Fig. 1c).

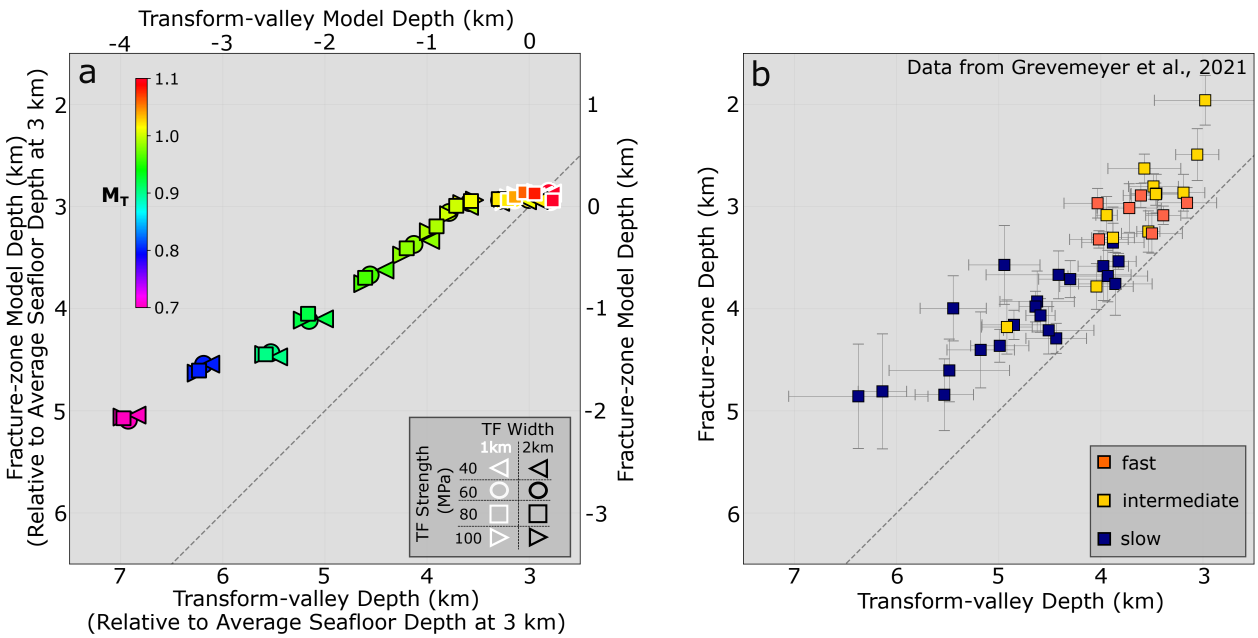

Fig. 4 | Depth difference between transform faults and adjacent fracture zones. (**a**) Model and (**b**) observed fracture-zone depth versus transform-valley depth (see Extended Data Fig. 1 for measurement details). Model and observed fracture zones are typically shallower than the transform valleys as seen by the vertical shift of the symbols relative to the dashed line, which marks the 1-to-1 ratio. In (a) colors denote M_T, symbol shape and outline color identify transform fault strength and width, respectively. Top and bottom horizontal axes are the same as in Fig. 3. (b) Global observations of transform valley and fracture zone depths (in km beneath sea level) grouped by spreading rate (fast > 8 cm/yr, intermediate 4–8 cm/yr and slow < 4 cm/yr).

Mechanisms that build transform topography

The model results above indicate a first-order control of intra-transform magmatism on transform fault and fracture zone topography (Fig. 3 & 4). When there is excess magmatism relative to the rate of far-field stretching, the stresses within the transform domain are generally compressive (Mode 1). This results in subtle and time-dependent curvature of the transform fault, which generates compressional transform ridges (Extended Data Fig. 3 a & b). When magma supply almost perfectly accommodates the far-field tectonic stretching, shear along the fault leads to tension across the transform and the formation of a shallow transform valley (Mode 2). In this case, stronger faults promote deeper valleys (Extended Data Fig. 2 and Extended Data Fig. 3 c-f) and little subsidence occurs along the adjacent fracture zones (Extended Data Fig. 1e). This across-transform shear-induced tension (Extended Data Fig. 3 c-f) arises as first hypothesized by analogy with a rubber band that is pinned on each side of a transform and is stretched due to the strike-slip motion of the fault [10]. The depth of the transform valley scales with this tensile stress, which increases with the shear strength of the transform fault (Extended Data Fig. 2 ($M_T \sim 1$) and Extended Data Fig. 3 c & e). The shear-driven tension only affects the active transform, but not the fracture zone, contributing to the depth difference between fracture zones and transforms for all models. Finally, when magma supply within the transform domain is insufficient to accommodate seafloor spreading, tectonic stretching creates deep transform valleys and subsided fracture zones (Extended Data Fig. 3 g & h). In this mode, the transform valley deepens more than the fracture zone because the transform is rheologically weaker due to the higher fault zone strain rates, allowing the far-field tectonic stretching to be preferentially partitioned into the transform domain. Another contributing factor for the depth difference is that the shear resistance of transform fault causes a slight (<1%) asymmetry in dike intrusions that open more toward the fracture zones.

Oceanic transform faults are observed to form over a range of spreading rates, average seafloor depths, fault lengths, and lithospheric thicknesses. To validate the first-order role of magma intrusion within the transform domain (M_T) on transform morphology, and to assess the broad applicability of our models, we further investigated the sensitivity of our model predictions to the aforementioned parameters. Of particular importance is the small change (< 87 m) in model topography due to differences in water overburden (Extended Data Fig. 4). This allows us to infer robust relationships when comparing our model results to observations, even though we assume a constant average seafloor depth of 3 km near mid-ocean ridges (double axes in Fig. 3d and Fig. 4a) [29–31]. Model predictions are also largely insensitive to variations in half spreading rates within the global range (1, 2, or 5 cm/yr), as well as a factor of ~2 difference in lithospheric thickness (4, 6 or 8 km) or transform fault length (32 or 62 km) (Extended Data Fig. 5). Specifically, we find that over this range of parameter space, predicted transform and fracture zone depths differ by only hundreds of meters, and reinforce the global trends shown in Fig. 3d and Fig. 4a. We therefore conclude that our model results robustly point to M_T as the primary control of oceanic transform morphology. Transform-valley depths show the greatest variability at slow spreading rates (averaged root mean square deviation of 695 m and 556 m in transform valley and fracture zone depths at spreading rates ≤ 40 km/Myr, Fig. 3e), which is only partially explained by the variability in the sensitivity tests (corresponding standard deviations among Mode 3 models are 128 m and 158 m, Fig. 3d, Extended Data Fig. 4 & 5 and Extended Data Table 2). Thus, we hypothesize that the scatter in the natural data is mainly due to greater variability in magma supply at slower spreading rates [11].

Overall, our model provides a mechanical basis for a first-order connection between magma supply and the morphologies of oceanic transform faults and their adjacent fracture zones. Further, this model makes several testable predictions that motivate future investigations. First, local seismicity, detailed seafloor geodesy, and high-resolution crustal magnetization may provide evidence for active magmatic dike intrusions within the transform domain. The predicted stress fields from our models (Extended Data Fig. 3 c & e) are consistent with anomalous focal mechanisms observed at some oceanic transform fault (e.g., thrust mechanism at transform side inside corners; oblique normal faulting adjacent to the transform valleys) [32,33]. Second, the dike near the ridge-transform intersection opens asymmetrically, with more material intruded toward the fracture zone side than the transform side. In nature, this could generate thicker crust on the fracture zone side, which is consistent with recent observations showing systematic higher residual mantle Bouguer anomalies indicating thinner crust at transform faults and inside corner regions as compared to the corresponding fracture zones and outside corner regions [34]. Finally, future seafloor geodetic studies might be able to resolve the spreading rate dependence of magmatic accommodated plate extension (M_T) within the transform domain, as well as shear-induce extension across the transform.

Acknowledgments: This work benefited from discussions with Eunseo Choi, Jean-Arthur Olive, and W. Roger Buck. We are also grateful for comments from #reviewers. This work was supported by National Science Foundation grants NSF-OCE #19-28776 to M.B. and X.T.; NSF-OCE #19-28804 to G.I., J.S.; and European Research Council Consolidator grant ERC CoG MAGMA #771143 to B.K., A.P.

Author contributions: Conceptualization: MB, GI, XT, JS; Methodology: BK, AP, JS, XT; Funding acquisition: MB, GI; Writing – original draft: XT, MB, GI; Writing – review & editing: XT, MB, GI, JS, BK, AP

Competing interests: Authors declare no competing interests.

Additional information

Supplementary information

Correspondence and requests for materials should be addressed to X. T. at email address: x.tian@bc.edu.

References:

1. Grevemeyer, I., Rüpke, L. H., Morgan, J. P., Iyer, K. & Devey, C. W. Extensional tectonics and two-stage crustal accretion at oceanic transform faults. *Nature* **591**, 402–407 (2021).
2. Buck, W. R., Lavier, L. L. & Poliakov, A. N. Modes of faulting at mid-ocean ridges. *Nature* **434**, 719–723 (2005).
3. Macdonald, K. C. Mid-ocean ridges: Fine scale tectonic, volcanic and hydrothermal processes within the plate boundary zone. *Annual Review of Earth and Planetary Sciences* **10**, 155–190 (1982).
4. Sykes, L. R. Mechanism of earthquakes and nature of faulting on the mid-oceanic ridges. *Journal of Geophysical Research* **72**, 2131–2153 (1967).
5. Wilson, J. T. A new class of faults and their bearing on continental drift. *Nature* **207**, 343–347 (1965).
6. Ryan, W. B. *et al*. Global multi-resolution topography synthesis. *Geochemistry, Geophysics, Geosystems* **10**, (2009).
7. Wessel, P. *et al*. The generic mapping tools version 6. *Geochemistry, Geophysics, Geosystems* **20**, 5556–5564 (2019).

8. Pockalny, R. A., Fox, P. J., Fornari, D. J., Macdonald, K. C. & Perfit, M. R. Tectonic reconstruction of the Clipperton and Siqueiros Fracture Zones: Evidence and consequences of plate motion change for the last 3 Myr. *J. Geophys. Res.* **102**, 3167–3181 (1997).

9. Zhang, F., Lin, J., Zhou, Z., Yang, H. & Morgan, J. P. Mechanism of progressive broad deformation from oceanic transform valley to off-transform faulting and rifting. *The Innovation* **3**, 100193 (2022).

10. Bercovici, D., Dick, H. J. B. & Wagner, T. P. Nonlinear viscoelasticity and the formation of transverse ridges. *J. Geophys. Res.* **97**, 14195 (1992).

11. Olive, J.-A. & Dublanchet, P. Controls on the magmatic fraction of extension at mid-ocean ridges. *Earth and Planetary Science Letters* **549**, 116541 (2020).

12. Detrick, R. S., White, R. S. & Purdy, G. M. Crustal structure of North Atlantic Fracture Zones. *Rev. Geophys.* **31**, 439 (1993).

13. Gregg, P. M., Lin, J., Behn, M. D. & Montési, L. G. J. Spreading rate dependence of gravity anomalies along oceanic transform faults. *Nature* **448**, 183–187 (2007).

14. Hooft, E. E. E., Detrick, R. S., Toomey, D. R., Collins, J. A. & Lin, J. Crustal thickness and structure along three contrasting spreading segments of the Mid-Atlantic Ridge, 33.5–35 N. *Journal of Geophysical Research: Solid Earth* **105**, 8205–8226 (2000).

15. Howell, S. M. *et al*. Seafloor expression of oceanic detachment faulting reflects gradients in mid-ocean ridge magma supply. *Earth and Planetary Science Letters* **516**, 176–189 (2019).

16. Olive, J.-A., Behn, M. D. & Tucholke, B. E. The structure of oceanic core complexes controlled by the depth distribution of magma emplacement. *Nature Geoscience* **3**, 491–495 (2010).

17. Tian, X. & Choi, E. Effects of axially variable diking rates on faulting at slow spreading mid-ocean ridges. *Earth and Planetary Science Letters* **458**, 14–21 (2017).

18. Behn, M. D. & Ito, G. Magmatic and tectonic extension at mid-ocean ridges: 1. Controls on fault characteristics. *Geochemistry, Geophysics, Geosystems* **9**, (2008).

19. Ito, G. & Behn, M. D. Magmatic and tectonic extension at mid-ocean ridges: 2. Origin of axial morphology. *Geochemistry, Geophysics, Geosystems* **9**, (2008).

20. Liu, Z. & Buck, W. R. Global trends of axial relief and faulting at plate spreading centers imply discrete magmatic events. *Journal of Geophysical Research: Solid Earth* **125**, e2020JB019465 (2020).

21. Olive, J.-A. *et al*. Sensitivity of seafloor bathymetry to climate-driven fluctuations in mid-ocean ridge magma supply. *Science* **350**, 310–313 (2015).

22. Tucholke, B. E., Behn, M. D., Buck, W. R. & Lin, J. Role of melt supply in oceanic detachment faulting and formation of megamullions. *Geology* **36**, 455–458 (2008).

23. Kaus, B. J. *et al*. Forward and inverse modelling of lithospheric deformation on geological timescales. in *NIC symposium* 299–307 (2016).

24. Schierjott, J. C. *et al*. How transform fault shear influences where detachment faults form near mid-ocean ridges. *Sci Rep* **13**, 9259 (2023).

25. Karson, J. A. & Dick, H. J. B. Tectonics of ridge-transform intersections at the Kane fracture zone. *Marine Geophysical Researches* **6**, 51–98 (1983).

26. Ren, Y., Geersen, J. & Grevemeyer, I. Impact of Spreading Rate and Age-Offset on Oceanic Transform Fault Morphology. *Geophysical Research Letters* **49**, e2021GL096170 (2022).

27. Crameri, F. *et al*. A comparison of numerical surface topography calculations in geodynamic modelling: an evaluation of the 'sticky air'method. *Geophysical Journal International* **189**, 38–54 (2012).

28. Kaus, B. J., Mühlhaus, H. & May, D. A. A stabilization algorithm for geodynamic numerical simulations with a free surface. *Physics of the Earth and Planetary Interiors* **181**, 12–20 (2010).

29. Dalton, C. A., Langmuir, C. H. & Gale, A. Geophysical and geochemical evidence for deep temperature variations beneath mid-ocean ridges. *Science* **344**, 80–83 (2014).

30. Richards, F. D., Hoggard, M. J., Cowton, L. R. & White, N. J. Reassessing the thermal structure of oceanic lithosphere with revised global inventories of basement depths and heat flow measurements. *Journal of Geophysical Research: Solid Earth* **123**, 9136–9161 (2018).

31. Stein, C. A. & Stein, S. A model for the global variation in oceanic depth and heat flow with lithospheric age. *Nature* **359**, 123–129 (1992).

32. Wilcock, W. S., Purdy, G. M. & Solomon, S. C. Microearthquake evidence for extension across the Kane transform fault. *Journal of Geophysical Research: Solid Earth* **95**, 15439–15462 (1990).

33. Wolfe, C. J., Bergman, E. A. & Solomon, S. C. Oceanic transform earthquakes with unusual mechanisms or locations: Relation to fault geometry and state of stress in the adjacent lithosphere. *Journal of Geophysical Research: Solid Earth* **98**, 16187–16211 (1993).

34. Guo, Z. *et al*. Disparate crustal thicknesses beneath oceanic transform faults and adjacent fracture zones revealed by gravity anomalies. *Geology* **51**, 300–304 (2023).

35. Lavier, L. L., Buck, W. R. & Poliakov, A. N. Factors controlling normal fault offset in an ideal brittle layer. *Journal of Geophysical Research: Solid Earth* **105**, 23431–23442 (2000).

36. Ballmer, M. D., van Keken, P. E. & Ito, G. Hotspots, large igneous provinces, and melting anomalies. in (Elsevier, 2015).

Methods

We use the open-source numerical code LaMEM (Lithosphere and Mantle Evolution Model) [23]; https://bitbucket.org/bkaus/lamem) for the three-dimensional geodynamic simulations. LaMEM employs a finite difference discretization scheme on a fully staggered grid, combined with a marker-in-cell approach to solve the mass and momentum conservation equations using the multigrid numerical method.

The oceanic lithosphere is simulated in a Cartesian model domain of 64 km in X-axis (along-transform) direction, 32 km in Y-axis (across-transform) direction and 8 km in the vertical Z-axis direction (Fig. 2). We assume regular cubic mesh grids with an edge length of 0.5 km. The model results are not sensitive to grid sizes smaller than 1 km. In the vertical Z direction, the base models are composed of 6 km of oceanic lithosphere underlying 2 km of "sticky-air". The "sticky-air" layer is assumed to has a viscosity of $10^{17} Pa \cdot s$. The boundary between the "sticky-air" and lithosphere forms an internal free surface [27,28] for tracking the development of topography. Left and right boundaries are pulled with a half spreading rate of *Vx* = 2 cm/yr. Top boundary is open to in-and-out flow. Other boundaries are shear traction-free and allow no normal in-and-out flow.

As described in Kaus et al. (2016) (ref [23]), the rheology of the lithosphere is assumed to be elasto-visco-plastic and the total deviatoric strain rate is calculated as:

$$\dot{\varepsilon}_{ij} = \dot{\varepsilon}_{ij}^{el} + \dot{\varepsilon}_{ij}^{vs} + \dot{\varepsilon}_{ij}^{pl} = \frac{\tau_{ij}^{J}}{2G} + \dot{\varepsilon}_{II}^{vs}\frac{\tau_{ij}}{\tau_{II}} + \dot{\varepsilon}_{II}^{pl}\frac{\tau_{ij}}{\tau_{II}} \qquad (1)$$

where $\dot{\varepsilon}_{ij} = \frac{1}{2}(\frac{\partial v_i}{\partial x_j} + \frac{\partial v_j}{\partial x_i}) - \frac{1}{3}\frac{\partial v_k}{\partial x_k}\delta_{ij}$ is the deviatoric strain rate tensor, in which x_i ($i = x, y, z$) denotes Cartesian coordinate in *i* direction, v_i is velocity in *i* direction, δ_{ij} is the Kronecker delta, $\tau_{ij} = \sigma_{ij} + P\delta_{ij}$ is the Cauchy stress deviator tensor (σ_{ij} is the Cauchy stress tensor, P is lithostatic pressure). The $\dot{\varepsilon}_{ij}^{el}$, $\dot{\varepsilon}_{ij}^{vs}$ and $\dot{\varepsilon}_{ij}^{pl}$ are the elastic, viscous and plastic components, respectively. $\tau_{ij}^{J} = \frac{\partial \tau_{ij}}{\partial t} + \tau_{ik}\omega_{kj} - \omega_{ik}\tau_{kj}$ is the Jaumann objective stress rate, and $\omega_{ij} = \frac{1}{2}(\frac{\partial v_i}{\partial x_j} + \frac{\partial v_j}{\partial x_i})$ is the spin tensor, $G = 40$ GPa is the elastic shear modulus, and the subscript "*II*" denotes the square root of the second invariant of the corresponding tensor.

The magnitude of the plastic strain rate ($\dot{\varepsilon}_{II}^{pl}$) is determined by enforcing the Drucker-Prager yield criterion:

$$\tau_Y = \sin(\varphi)P + \cos(\varphi)C \tag{2}$$

where τ_Y is the brittle yield strength of the oceanic lithosphere, in terms of the second invariant of the deviatoric stress tensor, φ is the friction angle of 30°, *P* is depth dependent lithostatic pressure and *C* is cohesion.

A marker-in-cell method is used to track material properties and material advection is implemented in a Eulerian kinematical framework. During advection, the elastic stress history from the previous time step (τ_{ij}^n) is corrected on the markers to account for the rigid-body rotation, and then interpolated on the edge and cell control volumes using a distance-based averaging to obtain the effective strain rates:

$$\dot{\varepsilon}_{ij}^{*} = \dot{\varepsilon}_{ij} + \frac{\tau_{ij}^{*}}{2G\Delta t} \tag{3}$$

where $\tau_{ij}^{*} = \tau_{ij}^{n} + \Delta t(\omega_{ik}\tau_{kj}^{n} - \tau_{ik}^{n}\omega_{kj})$ and Δt is the model time step.

The effective viscosity (η^*) and the updated deviatoric stresses (τ_{ij}) are computed from the effective strain rates using the standard quasi-viscous expression:

$$\tau_{ij} = 2\eta^* \dot{\varepsilon}^*_{ij}, \eta^* = min\left[\left(\frac{1}{G\Delta t} + \frac{1}{\eta_p}\right), \frac{\tau_Y}{2\dot{\varepsilon}^*_{II}}\right] \tag{4}$$

where $\eta_p = 10^{24} Pa \cdot s$ is the assumed viscosity for the lithospheric plate not at yield. The model setup of an ideal layer with constant thickness and viscosity as a way to isolate second-order effects of asthenosphere drag has been previously used for investigating factors that control normal faulting [35]. This helps reducing the complex competing effects that may complicate the model systematics.

Two mid-ocean ridge segments are offset by 32 km, between which a transform fault forms spontaneously as a result of plastic deformation following the Drucker-Prager yield criterion. The dike intrusion along each mid-ocean ridge segment is implemented as a zone of magmatic intrusion that accounts for a fraction, M, of the full plate separation rate $2 \cdot Vx$ [2,15,24]. For the ridge segments outside of the transform domain, we assume $M = 1$ such that the far-field tectonic extension is fully accommodated by dike intrusions and the topographic structure is not complicated by abyssal-hill-forming normal faults, which have been extensively investigated previously [18,19,21].

Dike intrusion is implemented within the transform domain based on observations that indicate variable magmatism along oceanic transform faults and fracture zones [1,12,13,34]. The fraction of magmatic intrusion in the transform domain is denoted as M_T to distinguish it from the M value ascribed to the ridge axis outside of the transform domain. At each of the transform magmatic zones, the rate of magmatic extension is $1/2M_T \cdot 2Vx$, and so $M_T \cdot 2Vx$ represents the integrated opening rate within the transform domain, which may have a different relationship with spreading rate than *M* does for ridge segments outside of the transform domain [11]. The transform domain width is set to be either 1 or 2 km, which is roughly consistent with a recent analysis [26] that yielded a global median transform fault width of 2.5 to 1.8 km when the corresponding ridge full spreading rate is higher than 8 cm/yr. This approach allows us to simulate the observed increase in transform magma supply with spreading rate [13].

Using this model setup, we investigate two primary controls on transform morphology: (1) M_T, and (2) transform fault shear strength. We measure model topography on evenly spaced along- and across-transform sampling profiles, from which we calculate the average along- and across- transform model topography (Extended Data Fig. 1 d, e, f for mean along- and Extended Data Fig. 1 g, h, i for mean across- transform topography for the three example cases shown in Fig. 3). Transform valley and fracture zone model depths (shown in Fig. 3d and Fig. 4a) are measured from the mean along-transform profiles [1], once the across-transform topography has reached steady state or is evolving slowly, typically within 10 million years of model time.

Data availability: All data are available in the main text or as Extended Data Figures and Tables.

Code availability: The open-source code LaMEM [23] used for the numerical models in this work is available at https://bitbucket.org/bkaus/lamem/src/master/. All newly coded features for transform domain dike intrusion are included in https://bitbucket.org/doha18/morlamem/src/transform_valley/src/. Input files for the base models and python plotting scripts can be found at https://bitbucket.org/doha18/morlamem/src/transform_valley/MOTFT-paper/.

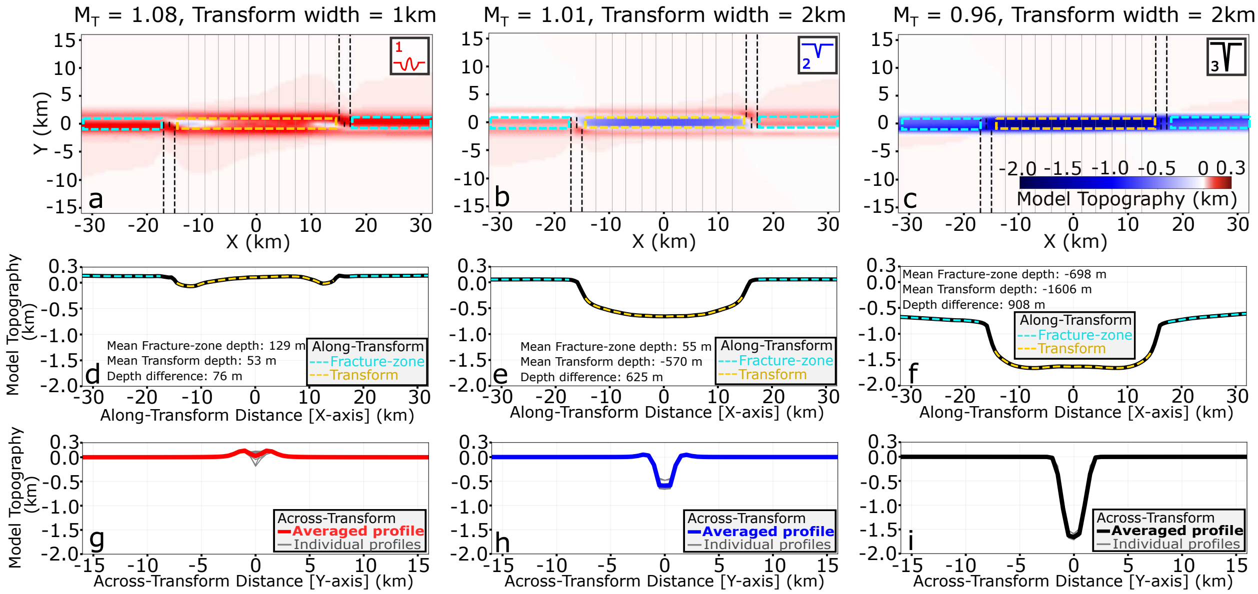

Extended Data Fig. 1 | Averaged along- and across- transform model topographic profiles for the three base model examples of Mode 1, 2, and 3 topographies shown in Fig. 3. (**a, b, c**) are map views of model topography for Modes 1, 2 and 3 respectively. (**d, e, f**) show the mean along- transform topographic profile for each case, with dashed cyan lines along the fracture-zones (highlighted with dashed cyan rectangles in a, b, c) and dashed yellow lines along the transforms (highlighted with dashed yellow rectangles in a, b, c). (**g, h, i**) show averaged across-transform topographic profiles from the 10 evenly spaced across-transform grey lines.

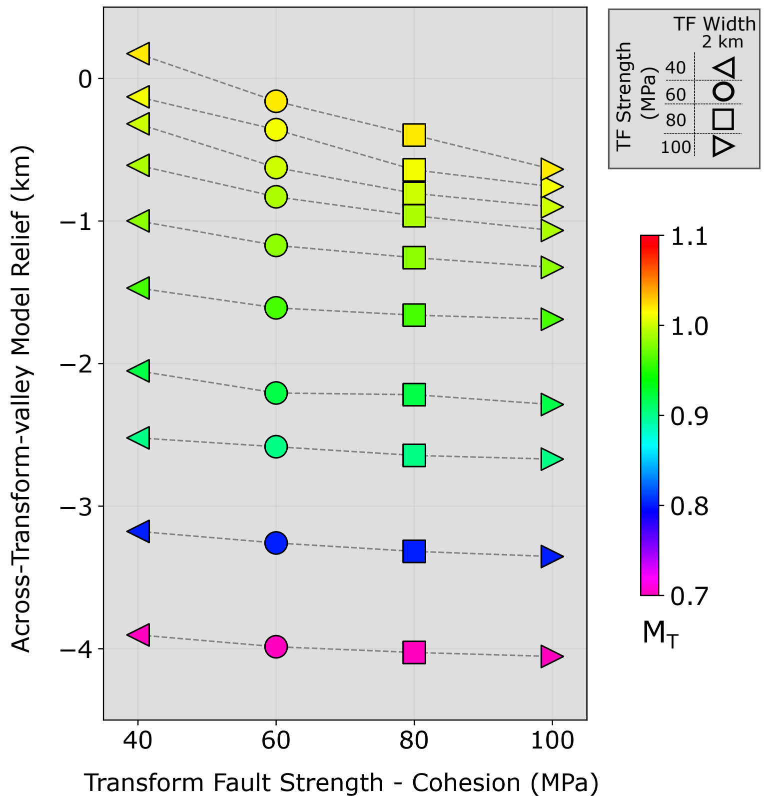

Extended Data Fig. 2 | Model across-transform valley relief as a function of M_T and transform fault (TF) strength varied the by different values of cohesion. Dashed lines illustrate trends of little or no dependence of transform valley depth on fault strength when far-field stretching dominates for the deep Mode 3 valleys (blue-green). By contrast, when there is little or no far-field tectonic extension ($M_T \approx 1$), shear-induced tension leads to low-relief valleys (Mode 2) (yellow-yellowish green), in which case transform valley depth increases with cohesion.

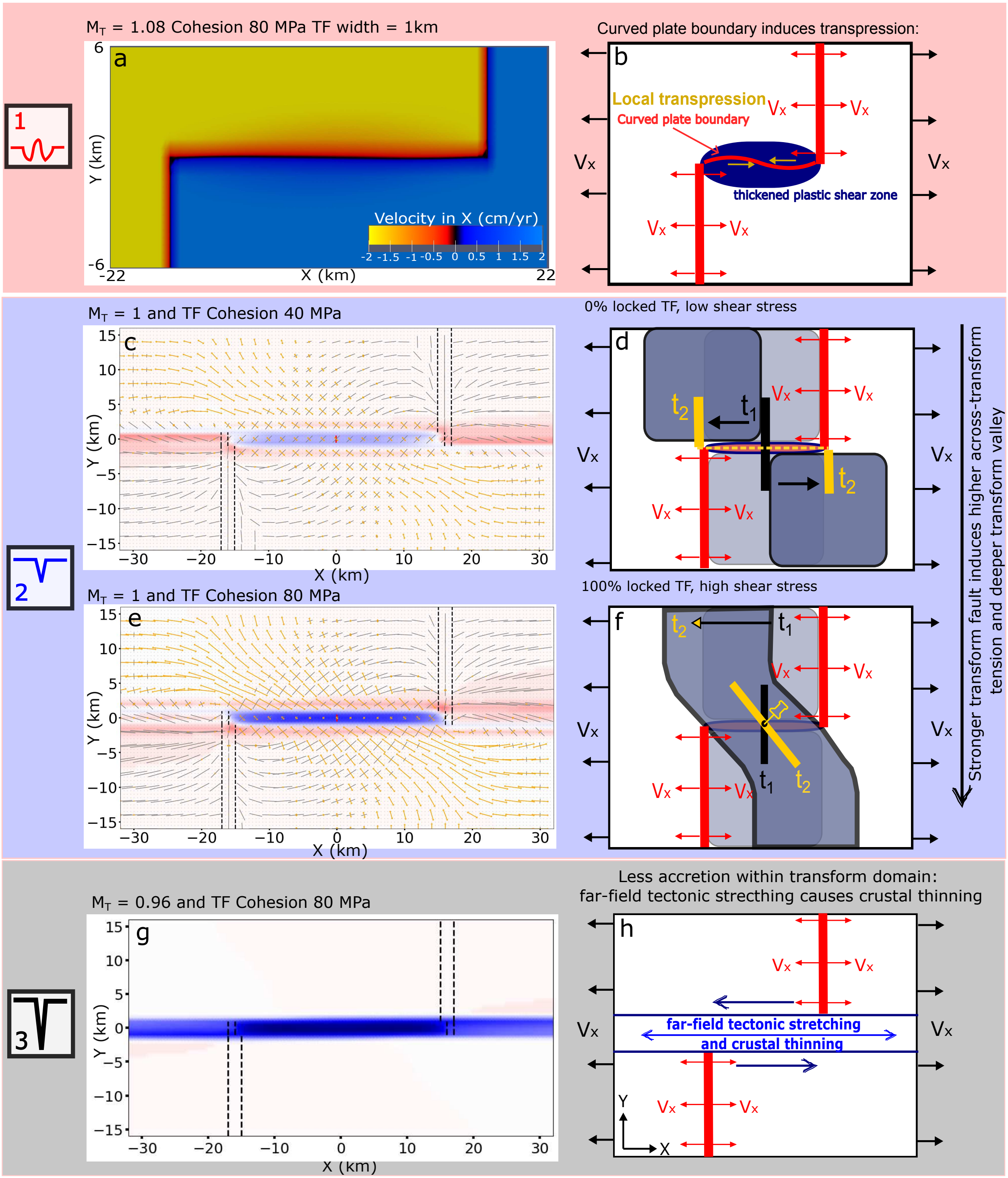

Extended Data Fig. 3 | Schematic diagrams illustrating the different mechanisms that control each mode of transform topography. For Mode 1, (**a**) shows a subset of mapview velocity in X direction at 2 km depth. Length in Y is exaggerated by a factor of two to better show the curving plate boundary at where the velocity in X is 0 cm/yr. This curving boundary coincides with transpression that leads to low-relief topographic ridges as shown schematically in (**b**). For Mode 2, (**c**) and (**e**) show magnitude (length of arrows/bars with the central reference red bar of 30 MPa) and direction of compressional (grey bars) and tensional (orange arrows) principal stresses overlying the model topography (pink shading).

Schematic end member scenarios to illustrate the underlying mechanics: (**d**) when the transform fault is frictionless, there is no shear stress induced by two plates sliding past each other from time 1 to time 2 and so no tension arises across the transform. (**f**) By contrast, when the transform fault is infinitely strong and allow no slip on the fault, the original black element at time 1 will be elongated at time 2 and experience shear-induced tension across the transform. For Mode 3, (**g**) model topography showing transform and fracture zone deepening due to lithospheric thinning from far-field tectonic stretching (**h**).

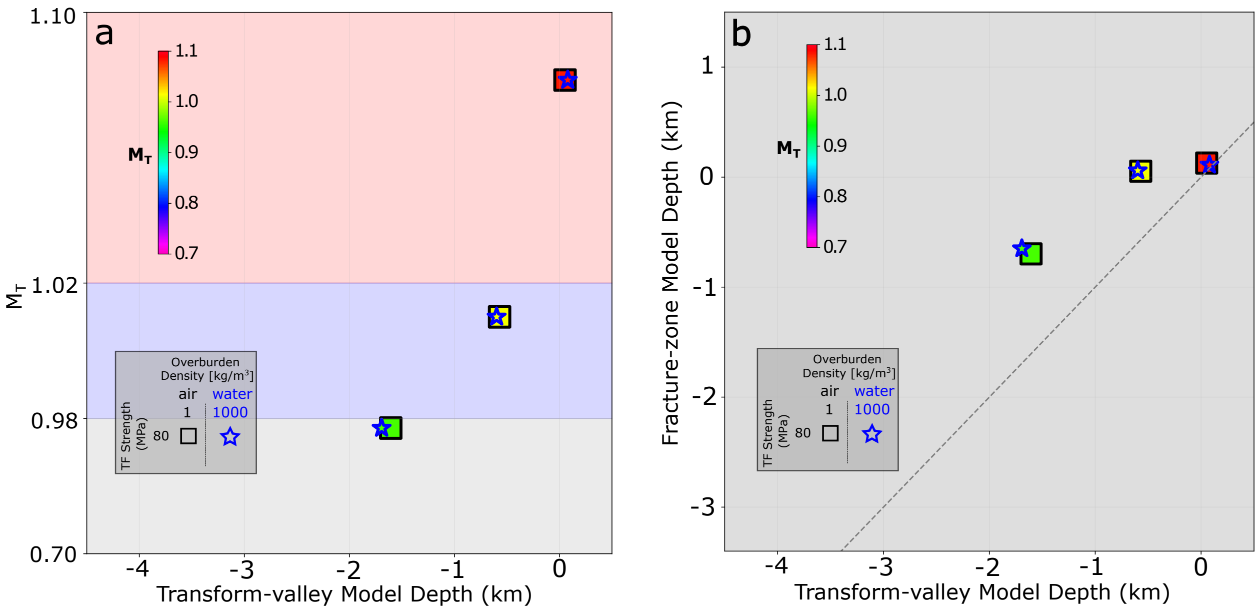

Extended Data Fig. 4 | Effect of seafloor overburden pressure on transform valley and fracture zone depth. The 3 example cases (rectangles) shown in Fig. 3, have negligible overburden pressure, but show very similar results to cases with 2 km of ocean water (density of 1000 kg/m^3) overburden (stars). Colors are for M_T. **a**) Transform valley model depth as a function of M_T as shown in Fig. 3d. **b**) Transform valley and fracture zone model depths as a function of M_T as shown in Fig. 4a. With water overburden, the transform and fracture zones are 26 m shallower while 17 m deeper for mode 1 case, 68 m deeper but 23 m shallower for mode 2 case and 120 m deeper but 115 m shallower for mode 3 case.

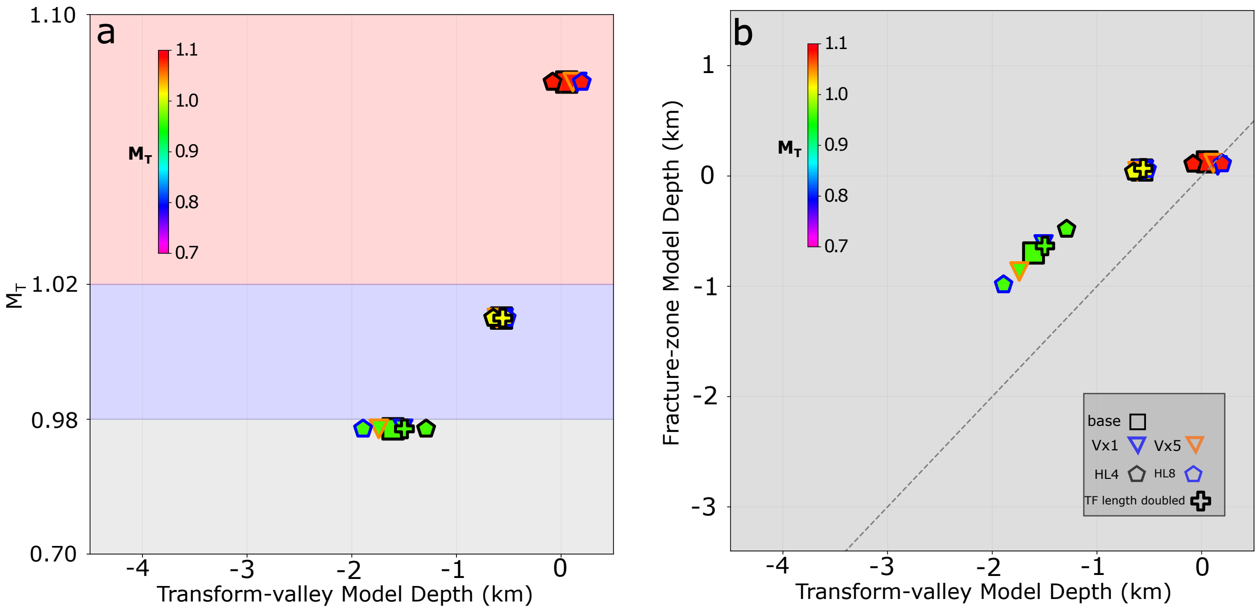

Extended Data Fig. 5 | Effect of spreading rate, lithospheric thickness and transform length on transform and fracture zone model depths. Symbol fill colors denote transform domain dike intrusion rate M_T. Rectangles are three base model examples shown in Fig. 3 that has half spreading rate of 2 cm/yr, lithospheric thickness of 6 km and transform fault length of 32 km. Triangles Vx1 (blue symbol stroke color) and Vx5 (orange symbol stroke color) indicate half spreading rates of 1 cm/yr and 5 cm/yr, respectively, keeping all other parameters the same as the base cases denoted with rectangles. Pentagons HL4 (black symbol stroke color) and HL8 (blue symbol stroke color) show results for lithospheric thickness of 4 km and 8 km, respectively. The crosses are for the 3 base cases, but with model domain in X and Y doubled and transform fault length increases from 32 to 62 km.

Extended Data Table 1. Model parameters and results shown in Fig. 3 & 4. Main controlling parameters are M_T and cohesion, and main model results are averaged fracture zone depth ("Avg FZ") and averaged along- and across- transform fault depth ("Avg TF" and "Avg across-TF") relative to the initial surface at 0 m, and depth difference between fracture zones and their adjacent transform ("FZ-TF").

#	M_T	Cohesion [MPa]	Transform width [km]	Overburden density [kg/m3]	Vx [cm/yr]	H_Litho [km]	TF Length [km]	Avg FZ [m]	Avg TF [m]	FZ-TF [m]	Avg across-TF [m]
1	0.7	40	2	1	2	6	32	-2042	-3841	1799	-3903
2	0.8	40	2	1	2	6	32	-1543	-3119	1576	-3177
3	0.9	40	2	1	2	6	32	-1472	-2454	982	-2521
4	0.92	40	2	1	2	6	32	-1100	-2005	905	-2051
5	0.96	40	2	1	2	6	32	-622	-1413	791	-1470
6	0.98	40	2	1	2	6	32	-332	-965	633	-999
7	0.99	40	2	1	2	6	32	1	-585	586	-609
8	1	40	2	1	2	6	32	41	-280	321	-318
9	1.01	40	2	1	2	6	32	56	-17	73	-129
10	1.02	40	2	1	2	6	32	58	97	-39	174
11	1.02	40	1	1	2	6	32	72	-49	121	-103
12	1.04	40	1	1	2	6	32	95	65	30	125
13	1.06	40	1	1	2	6	32	109	141	-32	203
14	1.08	40	1	1	2	6	32	99	194	-95	260
15	1.1	40	1	1	2	6	32	131	226	-95	290
16	0.7	60	2	1	2	6	32	-2092	-3926	1834	-3986
17	0.8	60	2	1	2	6	32	-1545	-3188	1643	-3258
18	0.9	60	2	1	2	6	32	-1431	-2530	1099	-2583
19	0.92	60	2	1	2	6	32	-1115	-2155	1040	-2206
20	0.96	60	2	1	2	6	32	-670	-1558	888	-1609
21	0.98	60	2	1	2	6	32	-371	-1129	758	-1171
22	0.99	60	2	1	2	6	32	-58	-784	726	-830
23	1	60	2	1	2	6	32	38	-584	622	-625
24	1.01	60	2	1	2	6	32	61	-289	350	-359
25	1.02	60	2	1	2	6	32	69	-5	74	-160
26	1.02	60	1	1	2	6	32	66	-143	209	-205
27	1.04	60	1	1	2	6	32	95	17	78	-126
28	1.06	60	1	1	2	6	32	110	49	61	121
29	1.08	60	1	1	2	6	32	50	207	-157	280
30	1.1	60	1	1	2	6	32	147	192	-45	273
31	0.7	80	2	1	2	6	32	-2073	-3973	1900	-4026
32	0.8	80	2	1	2	6	32	-1606	-3233	1627	-3317
33	0.9	80	2	1	2	6	32	-1447	-2580	1133	-2644
34	0.92	80	2	1	2	6	32	-1050	-2165	1115	-2218
35	0.96	80	2	1	2	6	32	-698	-1606	908	-1660
36	0.98	80	2	1	2	6	32	-409	-1199	790	-1257
37	0.99	80	2	1	2	6	32	-194	-907	713	-963
38	1	80	2	1	2	6	32	7	-714	721	-806
39	1.01	80	2	1	2	6	32	54	-570	624	-641
40	1.02	80	2	1	2	6	32	73	-297	370	-397
41	1.02	80	1	1	2	6	32	62	-207	269	-322
42	1.04	80	1	1	2	6	32	94	-139	233	-236
43	1.06	80	1	1	2	6	32	139	-46	185	-182
44	1.08	80	1	1	2	6	32	128	53	75	135
45	1.1	80	1	1	2	6	32	59	231	-172	324
46	0.7	100	2	1	2	6	32	-2061	-3986	1924	-4054
47	0.8	100	2	1	2	6	32	-1631	-3260	1629	-3353
48	0.9	100	2	1	2	6	32	-1448	-2599	1151	-2670
49	0.92	100	2	1	2	6	32	-1112	-2221	1109	-2287
50	0.96	100	2	1	2	6	32	-755	-1629	874	-1689
51	0.98	100	2	1	2	6	32	-475	-1248	773	-1325
52	0.99	100	2	1	2	6	32	-247	-986	739	-1066
53	1	100	2	1	2	6	32	-80	-788	708	-901
54	1.01	100	2	1	2	6	32	29	-659	688	-759
55	1.02	100	2	1	2	6	32	63	-535	598	-637
56	1.02	100	1	1	2	6	32	49	-244	293	-396
57	1.04	100	1	1	2	6	32	84	-199	283	-346
58	1.06	100	1	1	2	6	32	108	-128	236	-251
59	1.08	100	1	1	2	6	32	128	-31	159	-153
60	1.1	100	1	1	2	6	32	137	66	71	155

Extended Data Table 2.

Model parameters and results for sensitivity tests. Tested parameters are highlighted with bold fonts and are underlined. For models with transform length of 62 km, model domain size in X and Y axes are doubled to 128 and 64 km.

#	M_T	Cohesion [MPa]	Transform width [km]	Overburden density [kg/m³]	Vx [cm/yr]	H_Litho [km]	Transform Length [km]	Avg FZ [m]	Avg TF [m]	FZ-TF [m]
BASE MODE1	**1.08**	80	1	1	2	6	32	128	53	75
	1.08	80	1	**1000**	2	6	32	111	79	32
	1.08	80	1	1	**1**	6	32	96	153	-57
	1.08	80	1	1	**5**	6	32	117	111	5
	1.08	80	1	1	2	**4**	32	109	-82	191
	1.08	80	1	1	2	**8**	32	112	197	-85
	1.08	80	1	1	2	6	**62**	-162	637	-799
BASE MODE2	**1.01**	80	2	1	2	6	32	54	-570	624
	1.01	80	2	**1000**	2	6	32	59	-598	657
	1.01	80	2	1	**1**	6	32	57	-550	607
	1.01	80	2	1	**5**	6	32	43	-614	657
	1.01	80	2	1	2	**4**	32	37	-649	686
	1.01	80	2	1	2	**8**	32	60	-521	581
	1.01	80	2	1	2	6	**62**	69	-558	627
BASE MODE3	**0.96**	80	2	1	2	6	32	-698	-1606	908
	0.96	80	2	**1000**	2	6	32	-650	-1693	1043
	0.96	80	2	1	**1**	6	32	-621	-1510	889
	0.96	80	2	1	**5**	6	32	-866	-1742	875
	0.96	80	2	1	2	**4**	32	-481	-1290	809
	0.96	80	2	1	2	**8**	32	-985	-1892	907
	0.96	80	2	1	2	6	**62**	-634	-1497	863

Supplementary Text

1. <u>Sensitivity tests</u>

Globally, oceanic transform faults are associated with different spreading rates, fault lengths, seafloor depths, and lithospheric thicknesses. To test the robustness of our main conclusion that the transform domain magmatism plays a first-order role in controlling the transform topography, and to gauge the parameter space over which our results are applicable, we investigated the effects of different ocean water depths, half spreading rates, lithospheric thicknesses and transform lengths on transform and fracture zone morphologies (Extended Data Fig. 4 & 5, Extended Data Table 2).

1.1 Sensitivity to ocean water overburden

The base models presented in Fig. 3 & 4 assumed a 2-km "sticky-air" layer with a density of 1 kg/m^3, which results in negligible overburden pressure onto the modeled internal free-surface. In reality, the ocean water pressure on the seafloor increases with deeper seafloor at slower spreading rate mid-ocean ridges (Fig. 3e). Hence, we picked the 3 base cases (Fig. 3a, b, c) to test effects of sea water overburden on transform valley and fracture zone depths (Extended Data Fig. 4). With 2 km of water (with an assumed density of 1000 kg/m^3) overlying the model seafloor, the Mode 1 model (Fig. 3a) shows little change. The Mode 2 case (Fig. 3b) shows a 28 m deeper transform valley that changes from -570 m to -598 m relative to the initial surface at 0 m, and 4 m shallower fracture zones that changes from 54 m to 59 m relative to the initial surface at 0 m. The Mode 3 model (Fig. 3c) has 48 m of shallower fracture zones that changes from -698 m to -650 m but an 87 m deeper transform valley that changes from -1606 m to -1693 m. These differences are significantly smaller than the uncertainties in the data (error bars in Fig. 3e and Fig. 4b), which have averaged root mean square deviations of 614 m and 450 m for the measurements of the transform valley and fracture zone depths, respectively [1]. The limited influence of variable ocean water overburden on transform and fracture zone topography allows us to assume a mean seafloor depth of 3 km [29–31] when comparing the model transform and fracture zone depths with the observations (Fig. 3 & 4).

1.2 Sensitivity to variable half spreading rates

The base models shown in Fig. 3 & 4 assumed a half spreading rate *Vx* of 2 cm/yr; however, natural mid-ocean ridge systems have spreading rate that range from less than 1 cm/yr up to ~7 cm/yr (Fig. 3e). Hence, we used the 3 base cases (Fig. 3a, b, c) to test effects of variable half spreading rates of 1 cm/yr and 5 cm/yr shown as blue and orange symbol stroke triangles in Extended Data Fig. 5, respectively. There is no morphological mode change among models as a function of the imposed spreading rate. For the Mode 1 and Mode 2 cases, when half spreading rate is either decreased to 1 cm/yr or increased to 5 cm/yr, negligible changes can be identified in transform valley and fracture zone model depths. For the Mode 3 case, increasing half spreading rate from 2 cm/yr to 5cm/yr causes the average fracture zone depth to deepen by 168 m from -698 m to -866 and the average transform-valley depth to deepen by 136 m from -1606 m to -1742 m. Decreasing half spreading rate from 2 cm/yr to 1 cm/yr causes the average fracture zone model depth to become shallower by 77 m from -698 m to -621 m and the average transform-valley model depth to become shallower by 96 m from -1606 m to -1510 m. Even though faster spreading rate leads to deeper fracture zones and transform valleys for the Mode 3 cases, depth differences between transform and fracture zones remain similar and data clusters around the same trend (Extended Data Fig. 5b). Also, these variations are less than one-third of the aforementioned uncertainties in the data.

1.3 Sensitivity to variable lithospheric thickness

The base models shown in Fig. 3 & 4 assumed a lithospheric thickness of 6 km, which is subject to change as a function of seafloor spreading rate. Hence, we used the 3 base cases and tested the effects of variable lithospheric thickness on transform and fracture zone model topography (Extended Data Fig. 5). Again, Mode 1 and Mode 2 cases show negligible changes, but for the Mode 3 case, thicker lithosphere leads to deeper fracture zones and transform-valleys. When lithospheric thickness is increased from 6 km to 8 km, average fracture zone model depth becomes deeper by 287 m from -698 m to -985 and the average transform-valley model depth becomes deeper by 286 m from -1606 m to -1892 m. When lithospheric thickness decreases from 6 km to 4 km, average fracture zone model depth becomes shallower by 217 m from -698 m to -481 and the average transform-valley model depth becomes shallower by 316 m from -1606 m to -1290 m. The depth differences between the transform valley and fracture zone are almost invariant (Extended Data Fig. 5b) and the data clusters around the same trend as the main models (Fig. 4a). The changes are also less than the measured uncertainties in the data.

1.4 Sensitivity to transform fault length

Finally, to test the sensitivity to transform fault length, we increase the transform length from the value of 32 km used in the base cases to 62 km (crosses in Extended Data Fig. 5). To keep the aspect ratio between the transform fault and ridge segment the same, we doubled the model domain in the X and Y directions. The Mode 1 case is the most time-dependent, with the longer transform leading to higher transform topography by 584 m from 53 to 637 m and deeper fracture zones by 290 m from 128 m to -162 m. For the Mode 2 case, the longer transform results in negligible changes. For the Mode 3 case, the longer transform result in a shallower fracture zone and transform by 64 m (from -698 m to -634 m) and by 109 m (from -1606 m to -1497 m), respectively. The depth difference between the transform valley and fracture zone remains almost unchanged.

Note that the intermediate spreading rate data point (with a fracture zone depth of 1.96 km and transform depth of 2.98 km) that deviates from the model results in Fig. 4b is from the South East Indian Ridge at 78.4 °E, 38.55 °S. In this location average seafloor has been elevated by ~ 1 km as compared to the Vlamingh transform fault just southeastern (80.36 °E, 41.47 °S) to it due to the Amsterdam-St. Paul hotspot anomaly (e.g. ref [36]).

In summary, these sensitivity tests show that ocean water depth, half spreading rate, lithospheric thickness, and transform fault length play second-order roles in controlling the transform and fracture zone topography and in all cases their effects are smaller than the uncertainties in data measurements. These results support the first-order control of transform magmatism on modes of oceanic transform and fracture zone topography.

Supplementary References:

35. Lavier, L. L., Buck, W. R. & Poliakov, A. N. Factors controlling normal fault offset in an ideal brittle layer. *Journal of Geophysical Research: Solid Earth* **105**, 23431–23442 (2000).

36. Ballmer, M. D., van Keken, P. E. & Ito, G. Hotspots, large igneous provinces, and melting anomalies. in (Elsevier, 2015).